Science Advances
AAAS

advances.sciencemag.org/cgi/content/full/7/3/eabd6978/DC1

Supplementary Materials for

Direct coherent multi-ink printing of fabric supercapacitors

Jingxin Zhao, Hongyu Lu, Yan Zhang, Shixiong Yu, Oleksandr I. Malyi, Xiaoxin Zhao, Litong Wang, Huibo Wang, Jianhong Peng*, Xifei Li, Yanyan Zhang, Shi Chen, Hui Pan, Guichuan Xing, Conghua Lu, Yuxin Tang*, Xiaodong Chen*

*Corresponding author. Email: chenxd@ntu.edu.sg (X.C.); yxtang@fzu.edu.cn (Y.T.); pjhhj@sohu.com (J.P.)

Published 15 January 2021, *Sci. Adv.* **7**, eabd6978 (2021)
DOI: 10.1126/sciadv.abd6978

The PDF file includes:

Other Supplementary Material for this manuscript includes the following:

(available at advances.sciencemag.org/cgi/content/full/7/3/eabd6978/DC1)

Section S1. Supporting Notes

S1.1 XPS assignments for V_2O_5 electrode materials

Fig. S2a shows that the values of the three peaks in the literature were demanded to fit the V $2p^3$ peak (*36*). Fig. S2b exhibits that the O 1s spectra can be fitted into two typical characteristic peaks (530.3 and 531.0 eV), which belong to the metal-oxygen bonds and hydroxyl groups or oxygen vacancy defects, respectively (*37*).

S1.2 Structural characterization (SEM and TEM) of the VN electrode materials

Fig. S3a and b show that the as-prepared product embraces the one-dimensional nanowire structure when the as-prepared V_2O_5 was annealed under the NH_3 atmosphere, and the length of the samples can reach several of micrometers with a diameter of ≈ 200 nm. It can be observed that the as-prepared samples consisted of nanoparticles, and the highly porous microstructure was obtained, which is beneficial for the penetration of the electrolyte into the electrode and improving the capacitance characteristics (Fig. S3b). Fig. S3c exhibits the typical high-resolution TEM (HRTEM) image of the as-prepared sample. From Fig. S3c, the lattice spacing of 0.25 nm was obtained, which corresponds to the crystallographic plane of (200) VN. Moreover, the selected area electron diffraction (SAED) patterns show the monocrystalline nature of the porous VN nanowires (Fig. S3d).

S1.3 XRD assignments for VN/MWCNTs electrode materials

Fig. S6 exhibits that the five typical diffraction peaks are discovered at 2θ values of 37.9°, 44.2°, 64.1°, 77.1°, and 81.2°, which correspond to the crystallographic planes of (111), (200), (220), (311), and (222) of cubic VN. No other diffraction peaks ascribed to VO_x can be observed, demonstrating the product is pure VN. In addition, the diffraction peak at 2θ ≈ 25.6° confirms the existence of MWCNTs.

S1.4 XPS assignments for VN/MWCNTs electrode materials

In order to investigate the chemical states of the as-prepared samples, XPS was conducted. XPS confirms the formation of the VN/MWCNTs products (Fig. S7a). Moreover, the high-resolution XPS spectrum of the VN/MWCNTs is depicted in Fig. S7b-d. The main XPS peaks at 517.2, 524.7, and 530.1 eV that correspond to the binding energy of V $2p^3$, V $2p^1$, and O 1s electrons, respectively (Fig. S7b) (*39*). Additionally, the XPS peaks at 284.8 and 397.1 eV, corresponding to the C 1s of MWCNTs and the N 1s of VN, respectively (Fig. S7c, d) (*10*).

S1.5 Electrochemical performances of the as-prepared V_2O_5 NWs/MWCNTs and VN NWs/MWCNTs fiber electrode

To investigate the electrochemical properties of the 3D printing coaxial FASC device, the electrochemical performances of V_2O_5 NWs/MWCNTs fiber and VN NWs/MWCNTs fiber were measured by CV, GCD and EIS in a three-electrode system with a 1 M KOH electrolyte.

Fig. S12a exhibits the CV curves of the V_2O_5 NWs/MWCNTs fiber electrode in comparison with the pure MWCNTs fiber achieved at a scan rate of 5 mV s^{-1}. The signal from the pure MWCNTs fiber was negligible compared with the V_2O_5 NWs/MWCNTs fiber positive electrode. The CV curves of the prepared V_2O_5/MWCNTs fiber at different scan rates were exhibited in Fig. S12b, indicating the typical faradaic pseudocapacitive behavior (*3*). The reaction process can be described by the following equation: $V_2O_5 + xH^+ + xe^- \leftrightarrow H_xV_2O_5$. The maximum C_A value of 805.6 mF cm^{-2} at the current density of 1 mA cm^{-2}, and the specific capacitance value of 631.3 mF cm^{-2} is achieved at 10 mA cm^{-2}, demonstrating the excellent rate capability (Fig. S12c). Additionally, the small intrinsic resistance (R_b) value of ≈ 1.0 Ω was obtained (Fig. S12d). In order to achieve the 3D printing coaxial FASC device with excellent performance, the diameter of the VN NWs/MWCNTs fiber was rationally designed by the charge match, the diameter of 120 μm was observed from Fig. S5c.

As shown in Fig. S13a, the signal of the pure MWCNTs fiber was negligible in comparison with the VN NWs/MWCNTs fiber electrode. Fig. S13b reveals the CV curves of the VN NWs/MWCNTs fiber electrode taken between -1.2 and -0.2 V in 1.0 M KOH electrolyte, exhibiting the excellent electrochemical performance. The reaction process can be interpreted by the following equation: $VN + OH^- \leftrightarrow VN//OH^-$. From the GCD curves, the quasi-triangular shapes were obtained even at the current density of 10.0 mA cm^{-2}, exhibiting the pseudocapacitive behavior (Fig. S13c) (*33*). In addition, the VN NWs/MWCNTs fiber negative electrode embraces a smaller R_b value of approximately 1 Ω (Fig. S13d).

S1.6 The self-discharge tests of the 3D printing coaxial FASC device

Additionally, the self-discharge tests of the device are also executed. Fig. S16a exhibits the relationship between the leakage currents and time, and the leakage currents are recorded for the device charged to 1.6 V at the current density of 5 mA cm^{-2}. From Fig. S16a, the leakage current is relatively high in a short time, and then it will reduce with the increasing of time and eventually reach a stable current, demonstrating an appropriate self-discharge rate. Fig. S16b shows that the open-circuit voltage will decrease with the increasing of time, and ultimately achieve the steady-state voltage.

S1.7 The comparison of the areal, volumetric and gravimetric performance of the 3D printing coaxial FASC device

Fig. S19a, b exhibit that the device embraces the highest C_V and C_g of 27.83 F cm^{-3} and 59.26 F g^{-1}, respectively, which surpasses most of the previous work (*3, 5-9, 11, 14, 51, 52, 55*). Table S1 shows that the as-fabricated 3D printing coaxial FASC device embraces the highest E_A of 54.29 μWh cm^{-2}, the E_V of 9.88 mWh cm^{-3} and the E_g of 21.07 Wh kg^{-1}, which exceeds the most of the traditional FASC devices (*3, 5-11, 14, 16-18, 51-56*).

Section S2. Supporting Figures

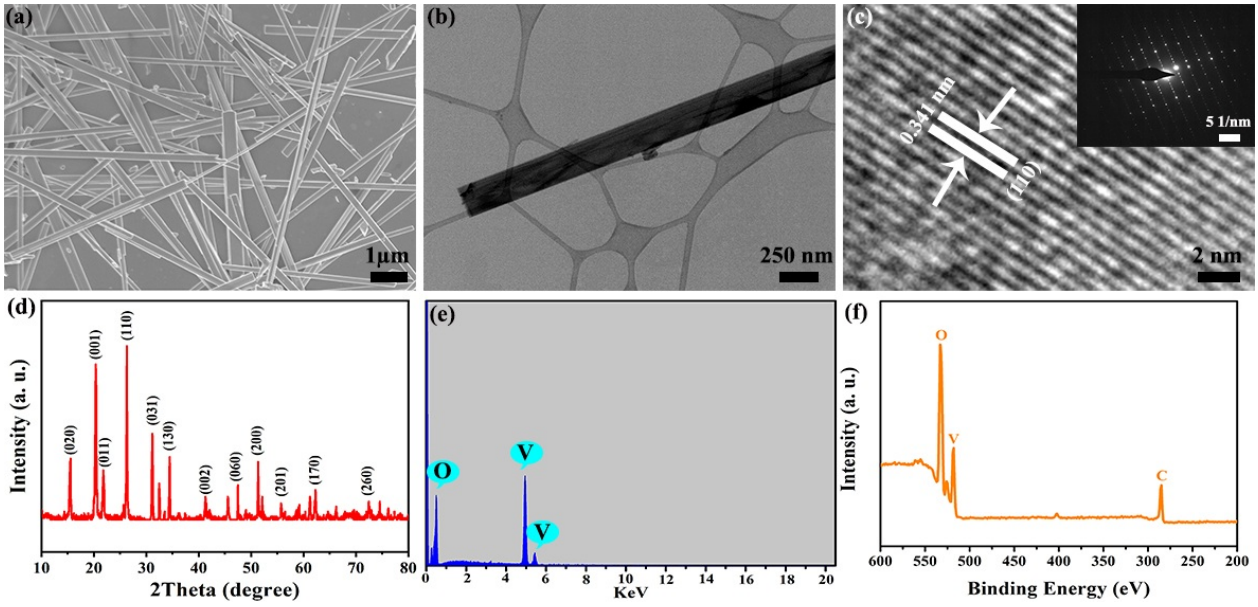

Fig. S1. Characterization of as-prepared V_2O_5. (a) SEM image. (b) Low-magnification TEM image. (c) High-resolution TEM image. Inset is the corresponding SAED pattern. (d) XRD pattern. (e) Energy dispersive spectroscopy (EDS) pattern. (f) XPS spectrum.

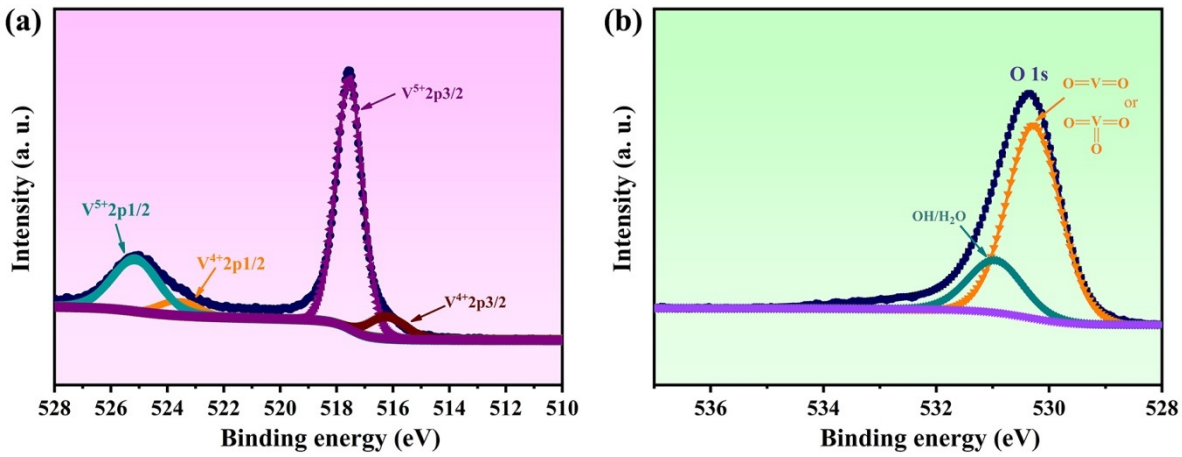

Fig. S2. XPS spectra and fitted curve. (a) V 2p and (b) O 1s of V_2O_5 samples.

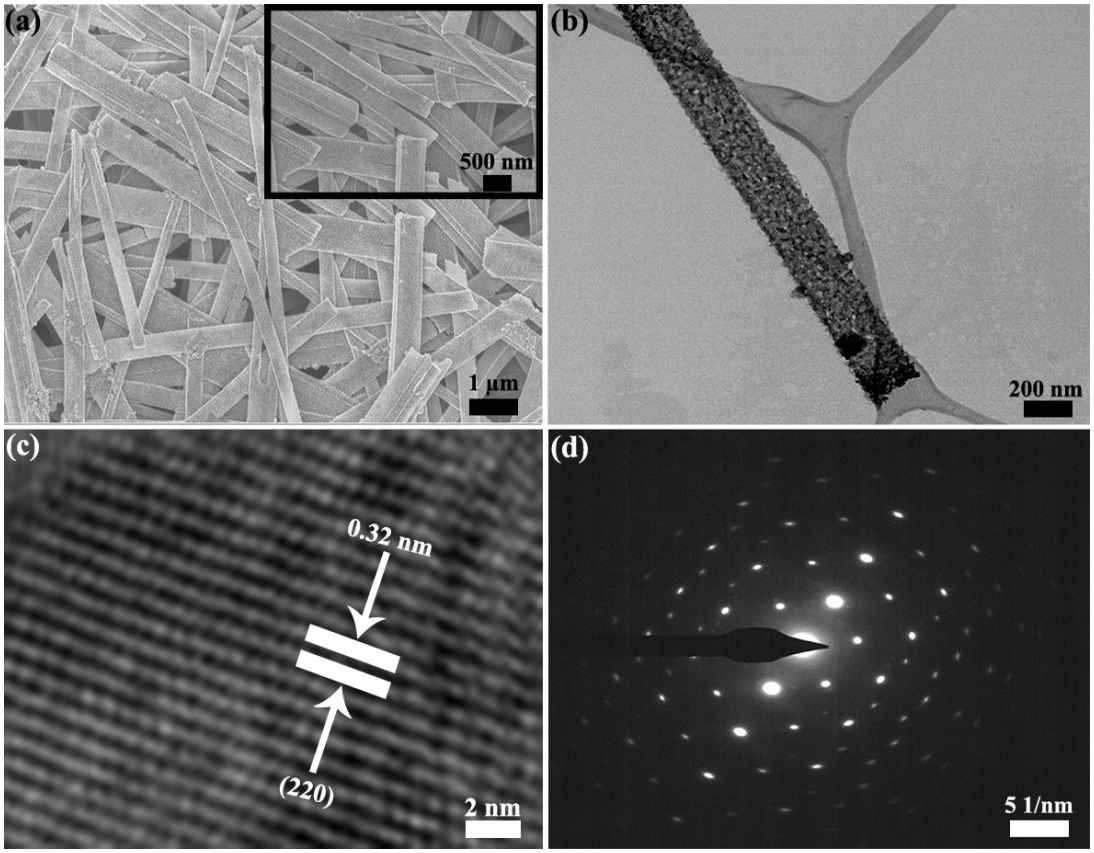

Fig. S3. Characterization of as-prepared VN. (a) Low-magnification SEM image, inset is a high-magnification SEM image. (b) Low-magnification TEM image. (c) High-resolution TEM image. (d) The corresponding SAED pattern.

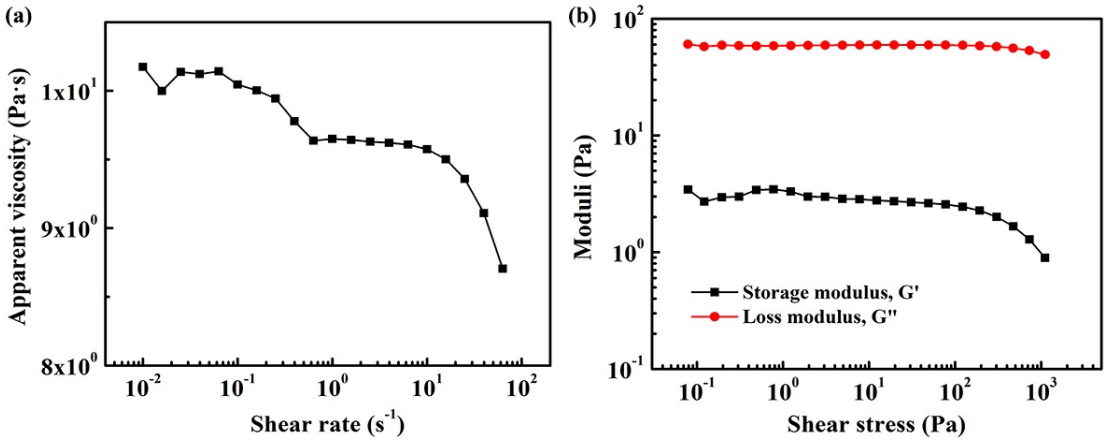

Fig. S4. Rheological properties of gel electrolyte ink. (a) Apparent viscosity as a function of shear rate for gel electrolyte ink. (b) Storage modulus, G′, and loss modulus, G″, as a function of shear stress for gel electrolyte ink.

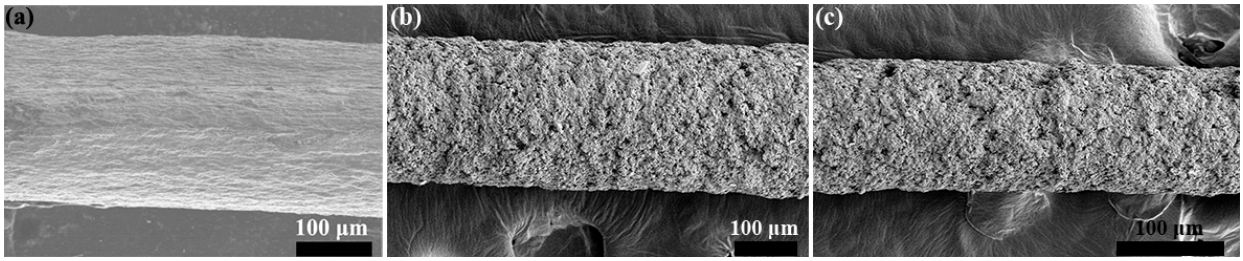

Fig. S5. Low-magnification SEM images of fiber electrodes. (a) MWCNTs fiber. (b) V_2O_5 NWs/MWCNTs fiber. (c) VN NWs/MWCNTs fiber.

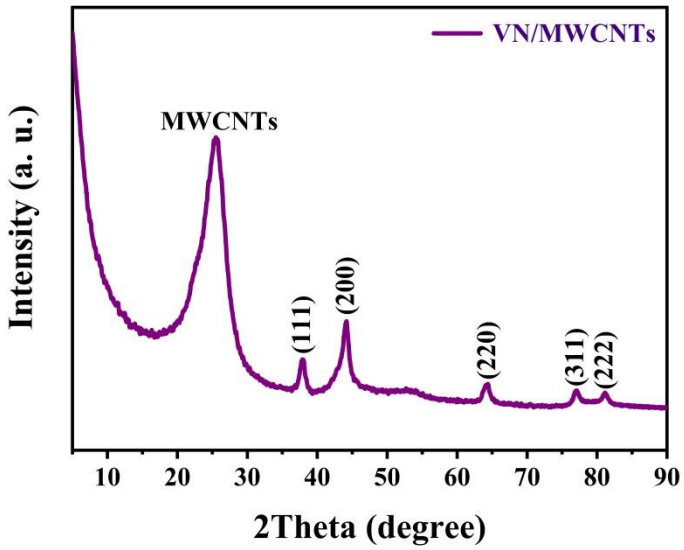

Fig. S6. XRD pattern of the as-fabricated VN/MWCNTs fiber.

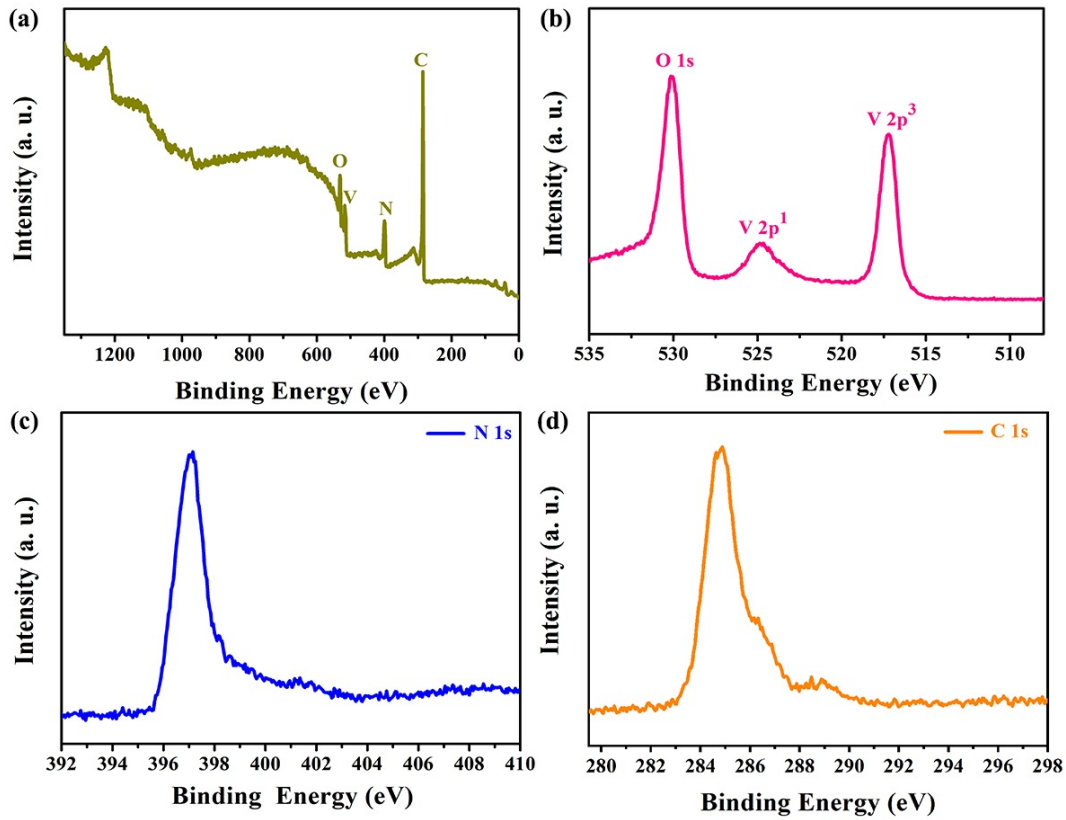

Fig. S7. XPS spectra of as-prepared VN/MWCNTs fiber. (a) Full-spectrum and High-resolution spectrum of (b) V 2p and O 1s, (c) N 1s, and (d) C 1s.

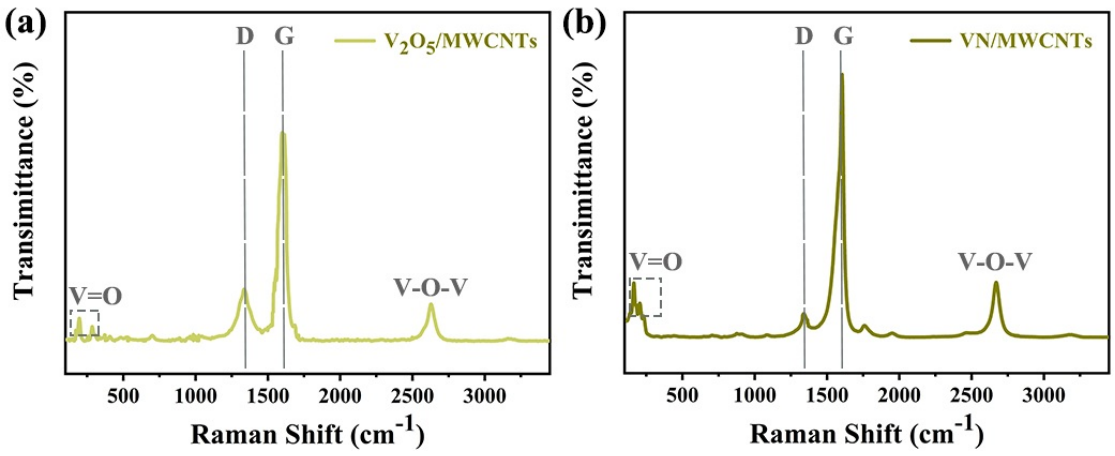

Fig. S8. Raman spectras of fiber electrodes. (a) V_2O_5 NWs/MWCNTs fiber. (b) VN NWs/MWCNTs fiber.

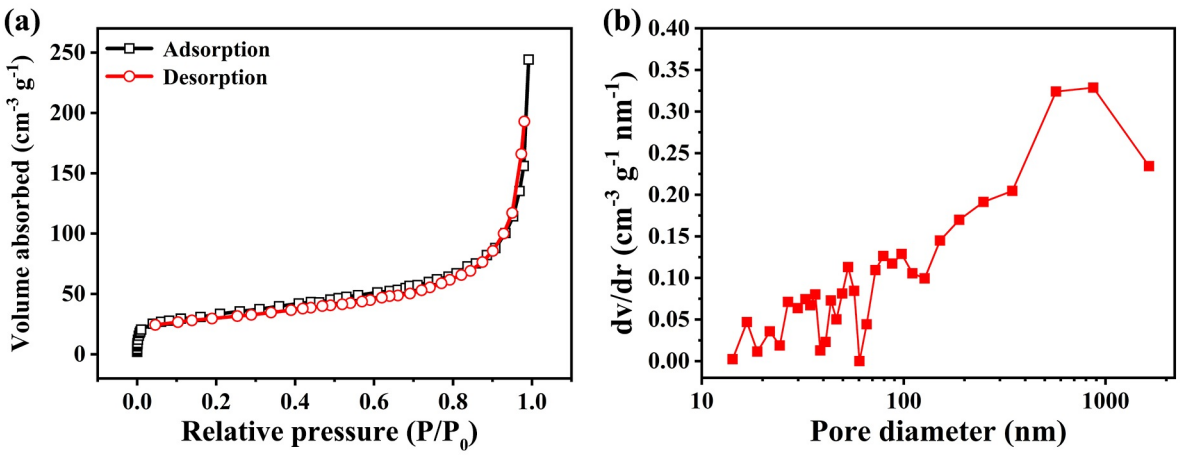

Fig. S9. BET test of the gel electrolyte. (a) N_2 adsorption/desorption isotherms. (b) Pore size distribution.

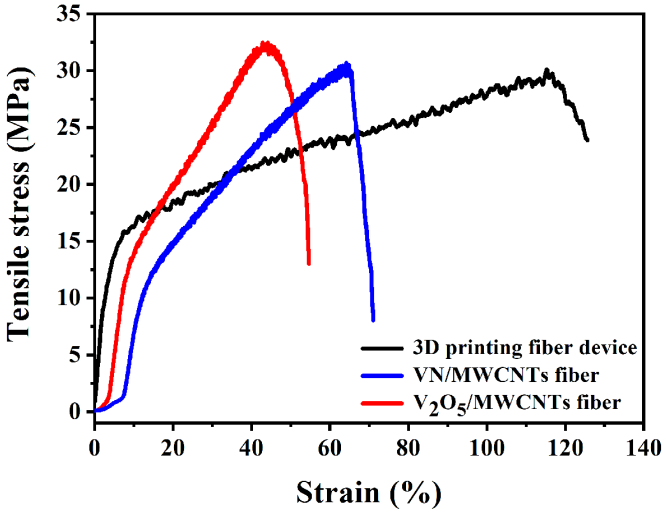

Fig. S10. The stress-strain performance of the printed fiber electrodes and devices.

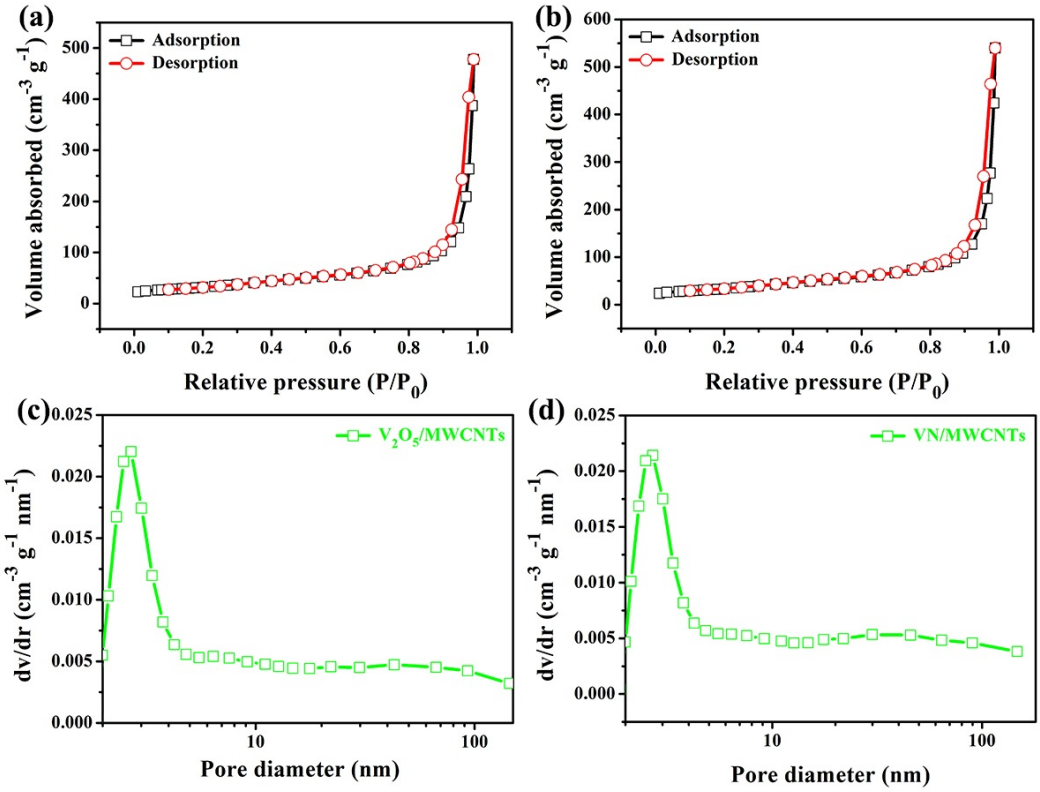

Fig. S11. BET tests of fiber electrodes. N_2 adsorption/desorption isotherms of the as-fabricated (a) V_2O_5 NWs/MWCNTs and (b) VN NWs/MWCNTs fiber. The pore size distribution of as-fabricated (c) V_2O_5 NWs/MWCNTs and (d) VN NWs/MWCNTs fiber.

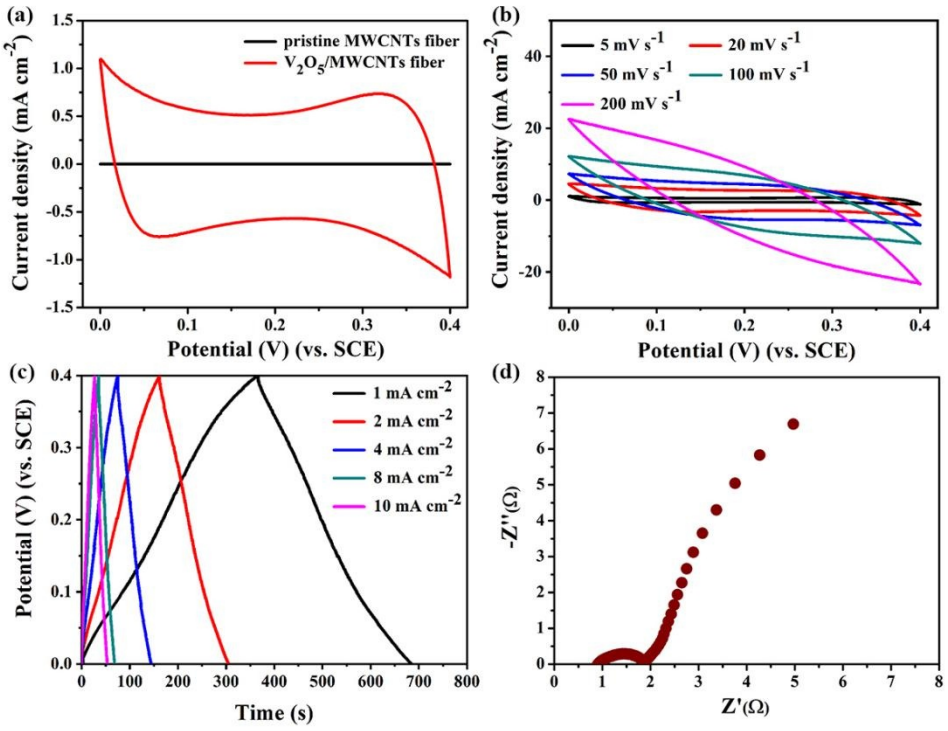

Fig. S12. Electrochemical performance of V_2O_5 NWs/MWCNTs fiber. (a) The CV curves of the V_2O_5 NWs/MWCNTs fiber in comparison with pure MWCNTs fiber at a scan rate of 5.0 mV s^{-1}. (b) The CV curves at the different scan rates. (c) The GCD curves at the different current densities. (d) Nyquist plot. It should be noted that Fig. S12b shows the different CV shape than the same material in the panel "a" is because of the existing of the polarization phenomenon when the scan rates increase.

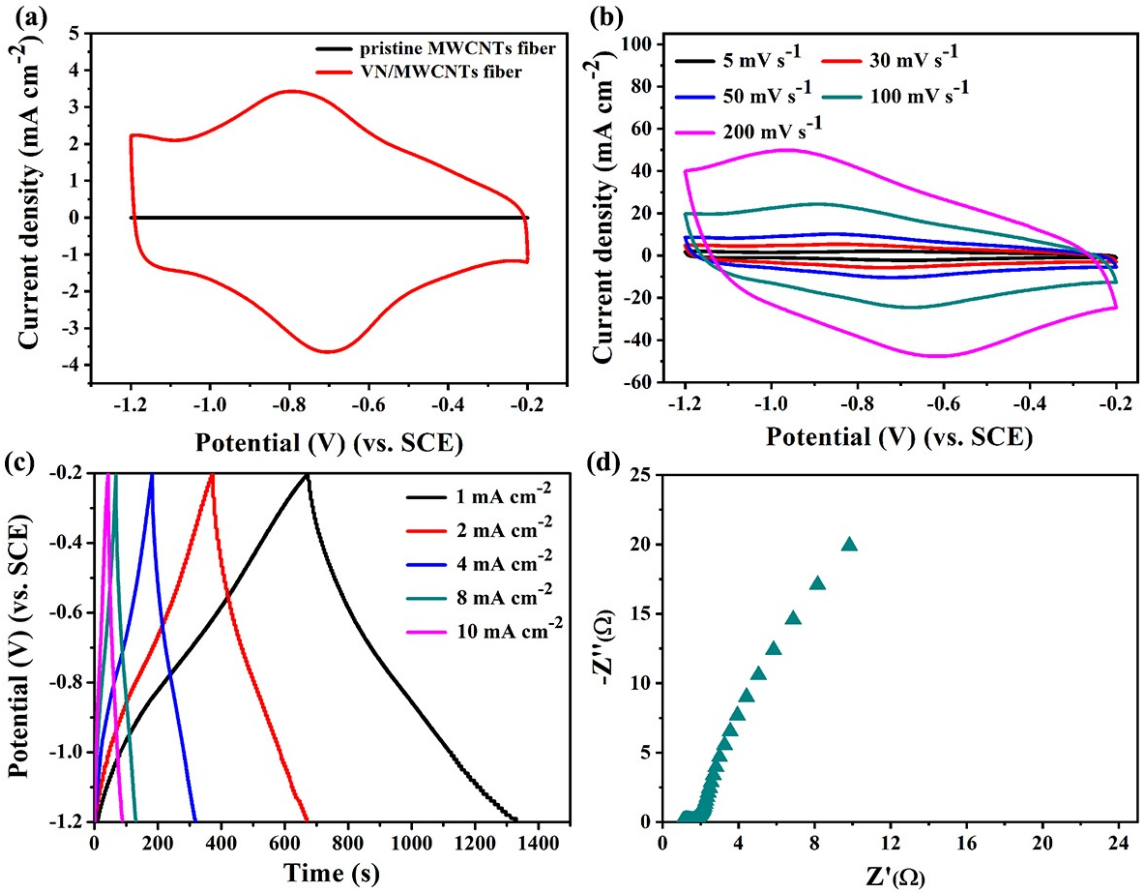

Fig. S13. Electrochemical performance of VN NWs/MWCNTs fiber. (a) The CV of the VN NWs/MWCNTs fiber in comparison with pure MWCNTs fiber. (b) The CV curves at the different scan rates. (c) The GCD curves at the different current densities. (d) Nyquist plot.

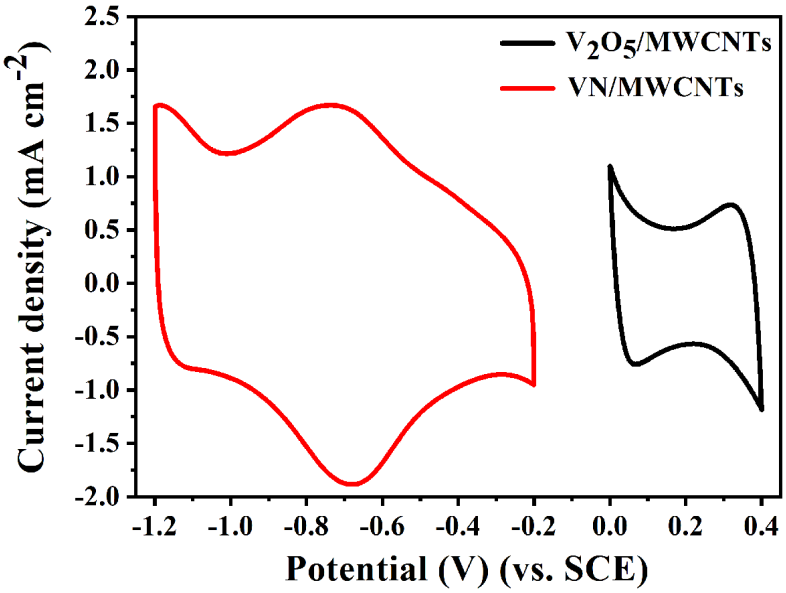

Fig. S14. The CV curves obtained for the V_2O_5 NWs/MWCNTs and VN NWs/MWCNTs fiber electrodes at 5.0 mV s^{-1}.

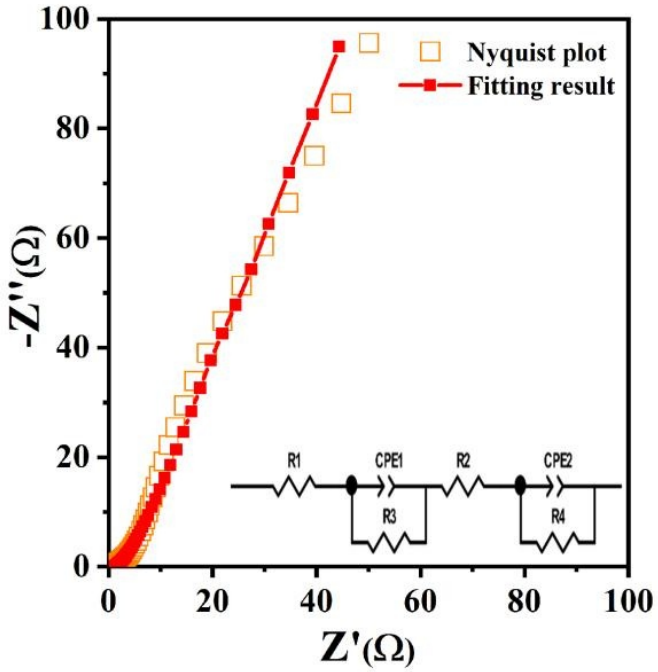

Fig. S15. Nyquist plot and the fitting result of the as-prepared 3D printing coaxial FASC device. The inset is the equivalent circuit of the device impedance.

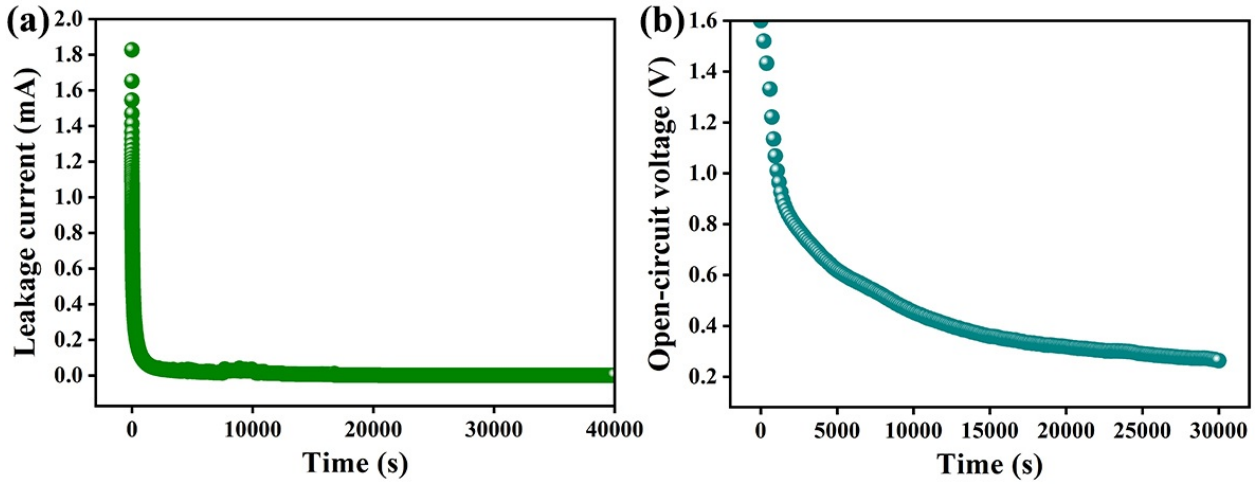

Fig. S16. Self-discharge performance of the as-prepared 3D printing coaxial FASC device. (a) Variation of leakage current with time. (b) Decay of open-circuit voltage for the device after being charged with the charge current density of 5 mA cm^{-2}.

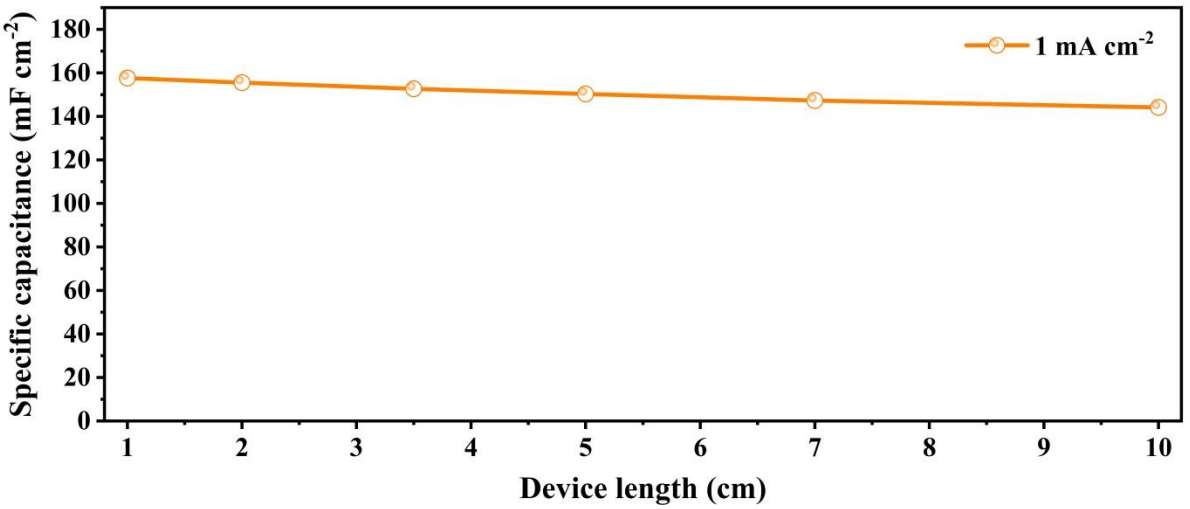

Fig. S17. The relationship between the electrochemical performances and the length of the devices.

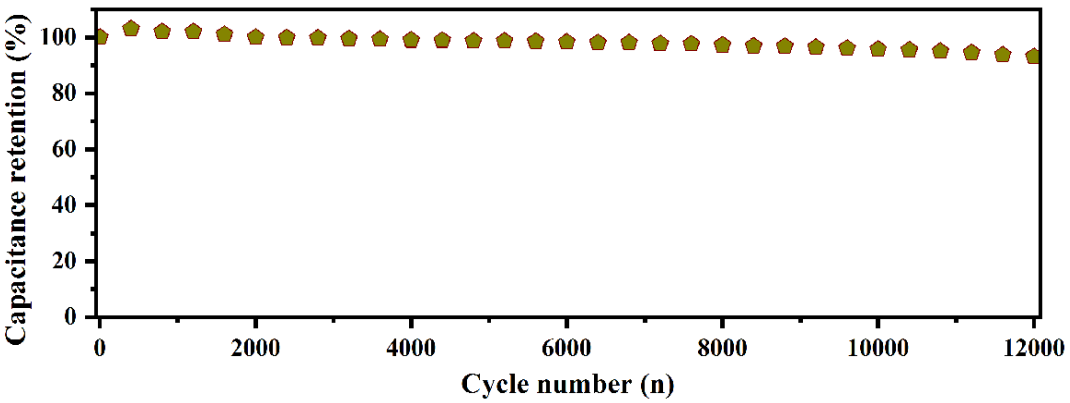

Fig. S18. Cyclic stability of the as-prepared 3D printing coaxial FASC device.

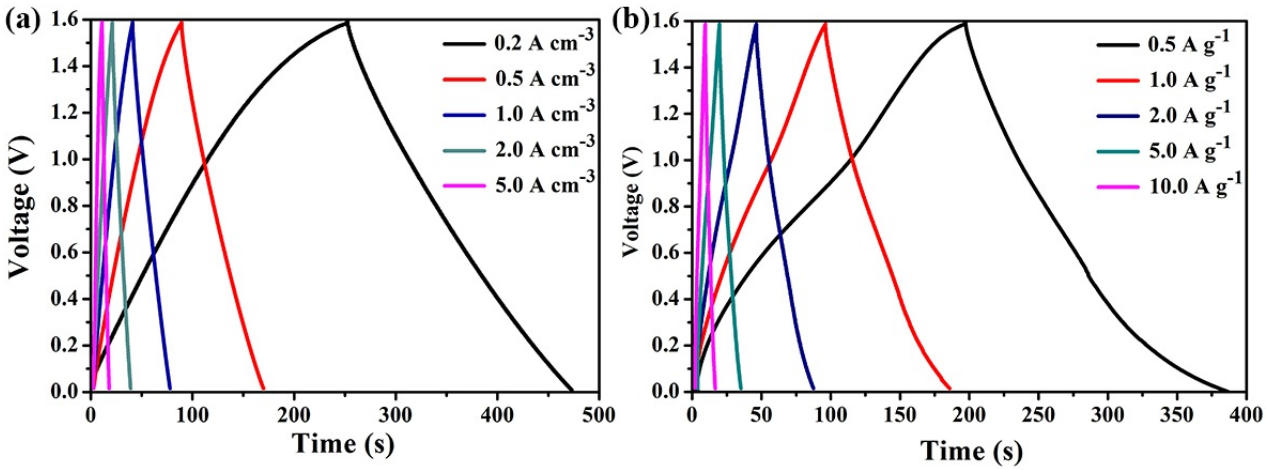

Fig. S19. GCD tests of the device. (a) GCD curves of the device at different volumetric current densities.

(b) GCD curves of the device at different gravimetric current densities.

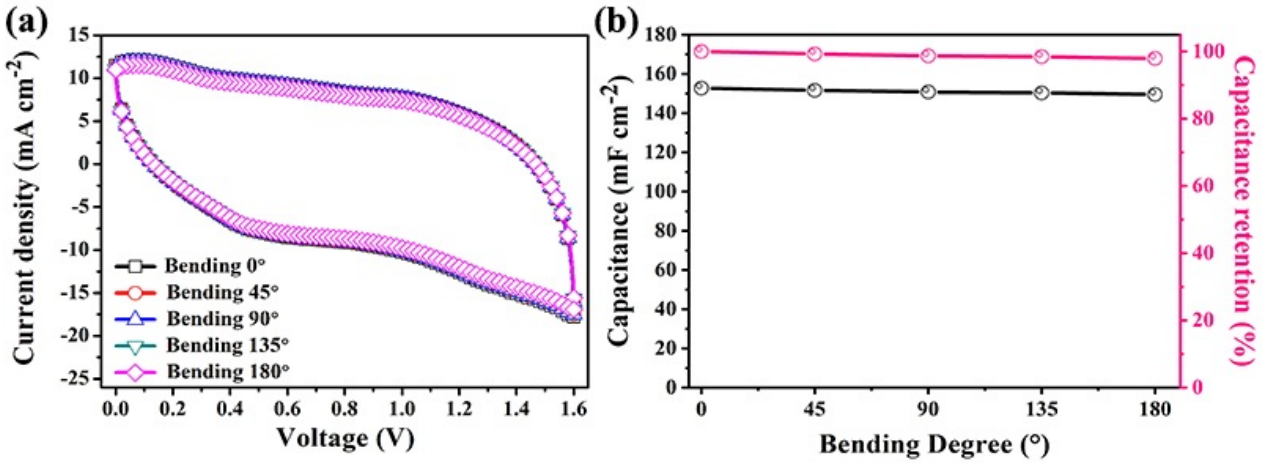

Fig. S20. Electrochemical performance of assembled 3D-printed coaxial FASC device under bending.

(a) CV curves of the printed device with different bending angles at the scan rate of 75 mV s^{-1}. (b) Capacitance and capacitance retention of the device under different bending angles.

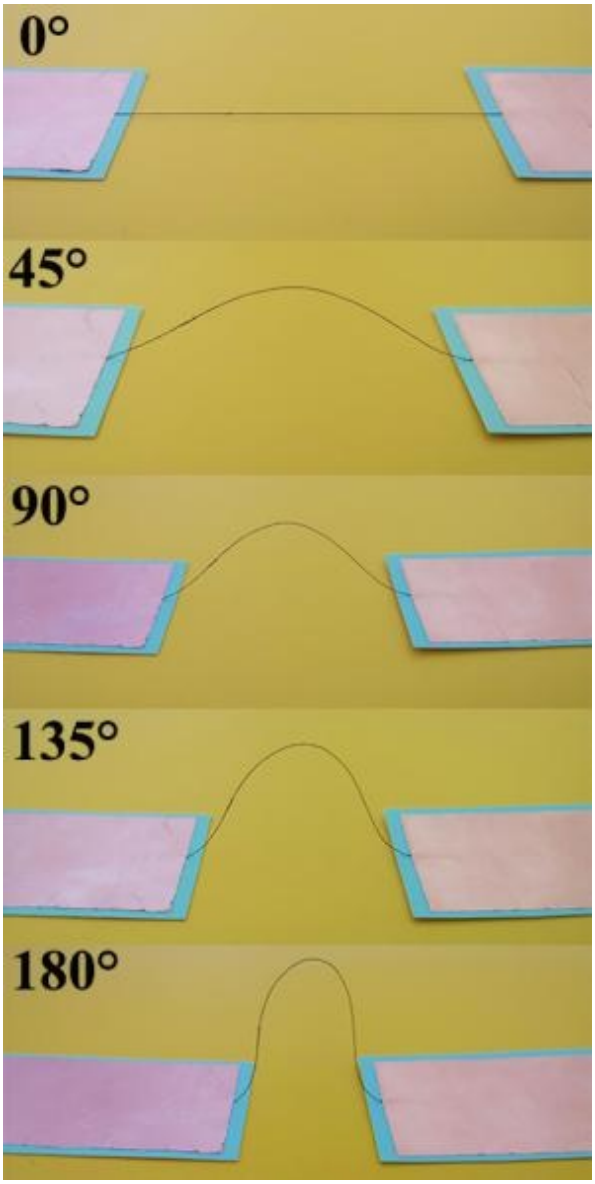

Fig. S21. The digital photos of the assembled 3D-printed coaxial FASC device at different bending.

Photo credit: Hongyu Lu, Xi'an University of Technology.

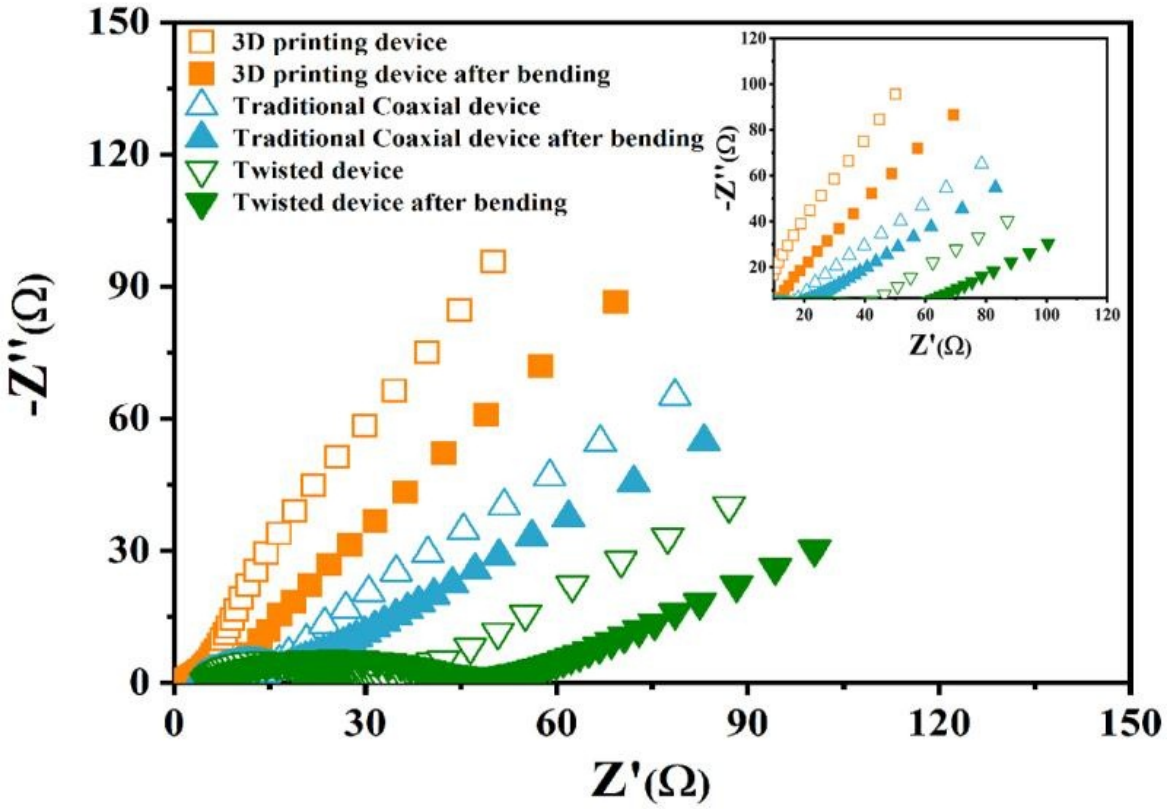

Fig. S22. Nyquist plots of the 3D printing coaxial FASC device, and the as-fabricated FASC with twisted and the traditional coaxial architectures before and after 3,000 cycles of bending.

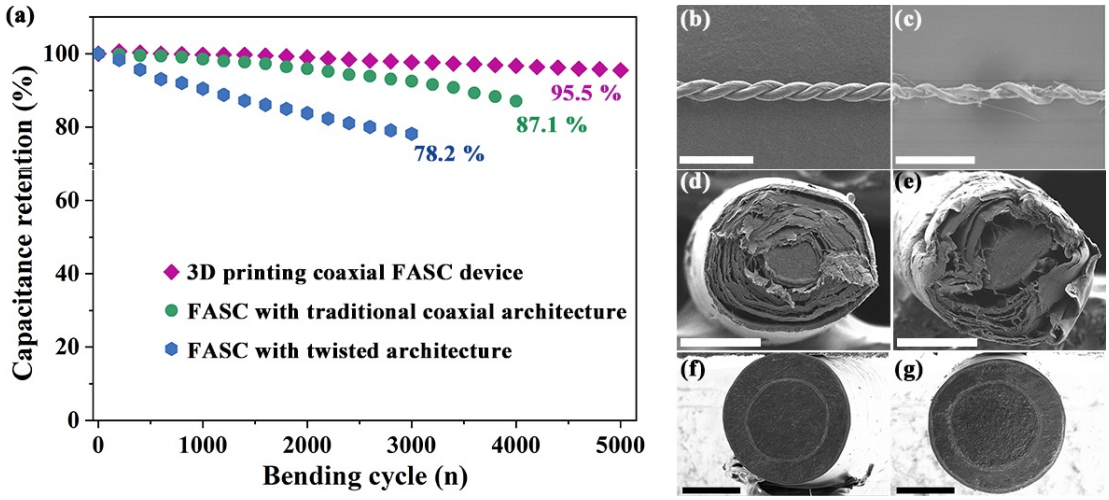

Fig. S23. Comparison of flexible performance of three kinds of fiber-shaped device. (a) The comparison of the capacitance retention of the 3D printing coaxial FASC device, and the as-fabricated FASC with twisted and the traditional coaxial architectures after bending cycles. The SEM images of the FASC device with the twisted architecture (b) and (c), the FASC device with the traditional coaxial architecture (d) and (e), and the 3D printing coaxial FASC device before and after bending (f) and (g). Scale bars: (b-g) 250 μm.

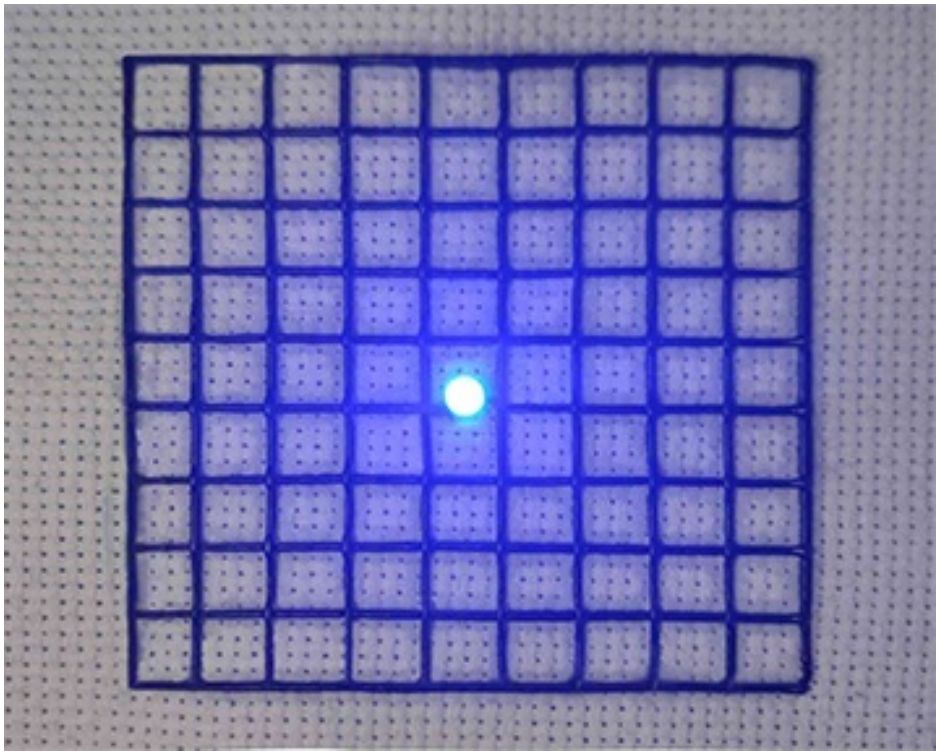

Fig. S24. Photograph of a 3.0 V blue LED illuminated by the charged energy textile consisting of our 3D printed coaxial FASC device. Photo credit: Yan Zhang, Nankai University.

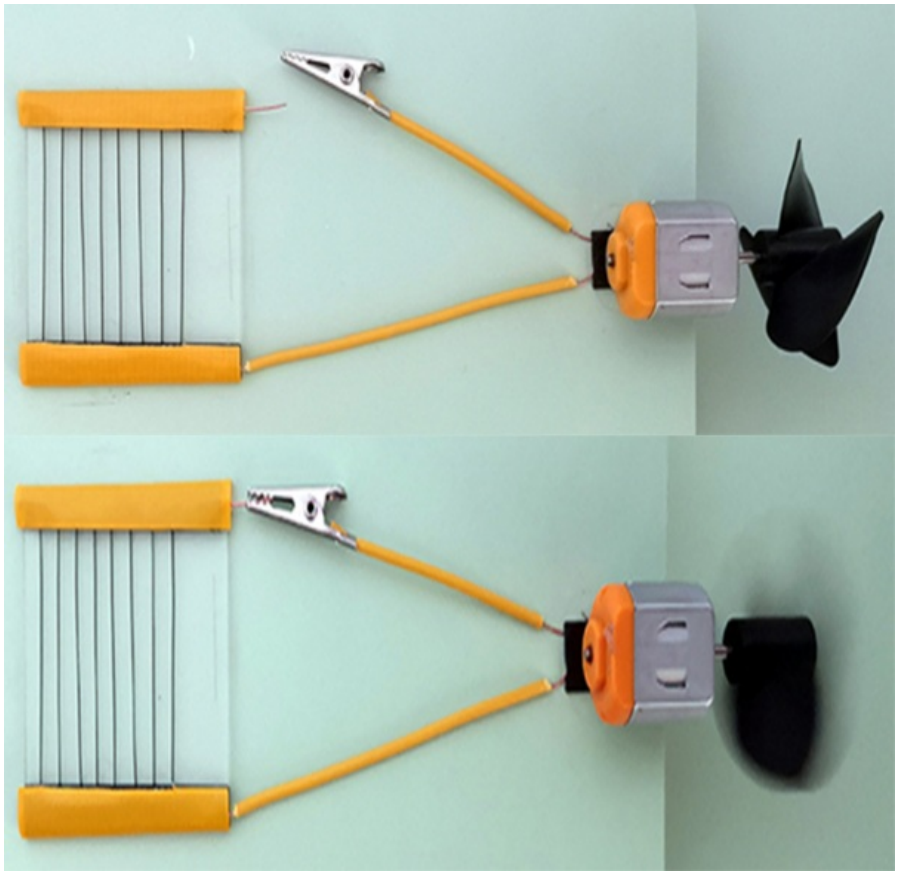

Fig. S25. Photographs of the chip-based FASC device to power the movements of pinwheel. Photo credit: Hongyu Lu, Xi'an University of Technology.

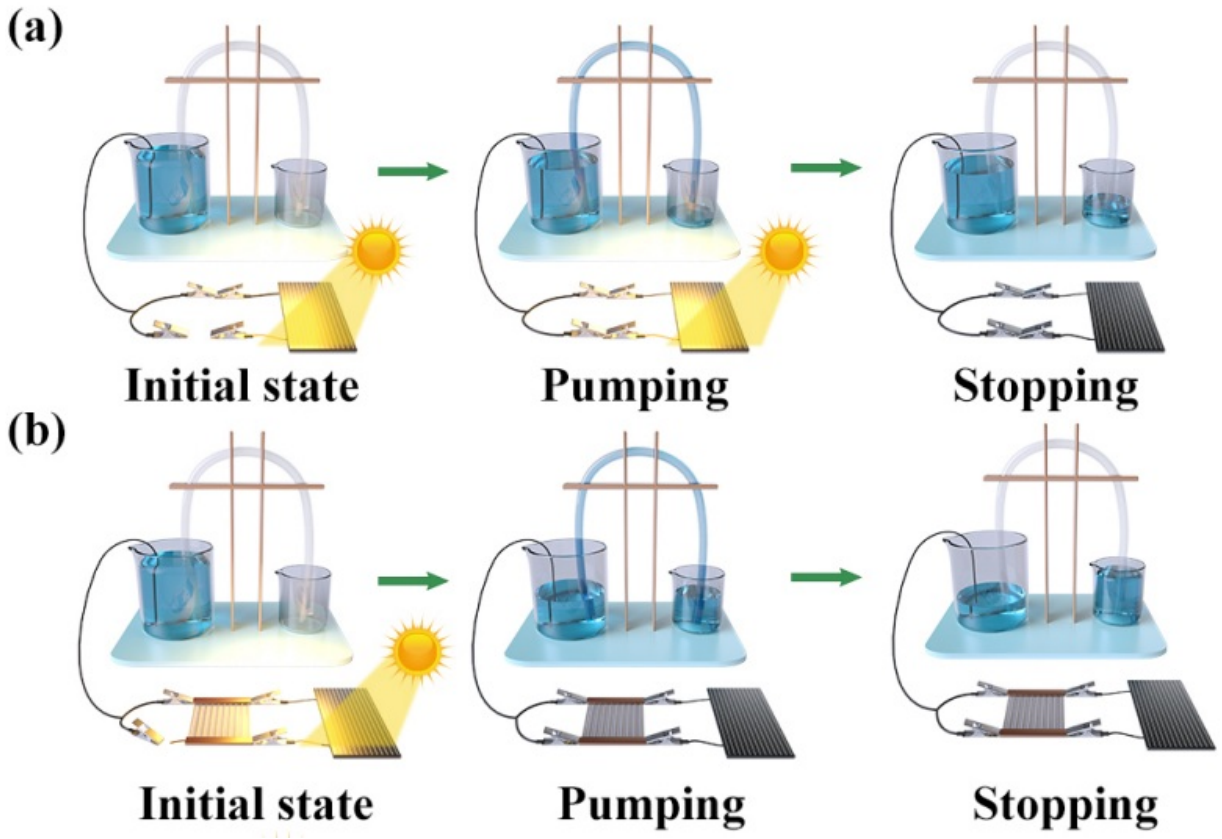

Fig. S26. Schematic diagram of water pumping system with solar cell and self-powered system. (a) Schematic diagram of water pumping prototype with solar cell only. (b) Schematic diagram of water pumping prototype with the self-powered configuration including chip-based FASC device and solar cell. Photo credit: (a and b) Jingxin Zhao, University of Macau.

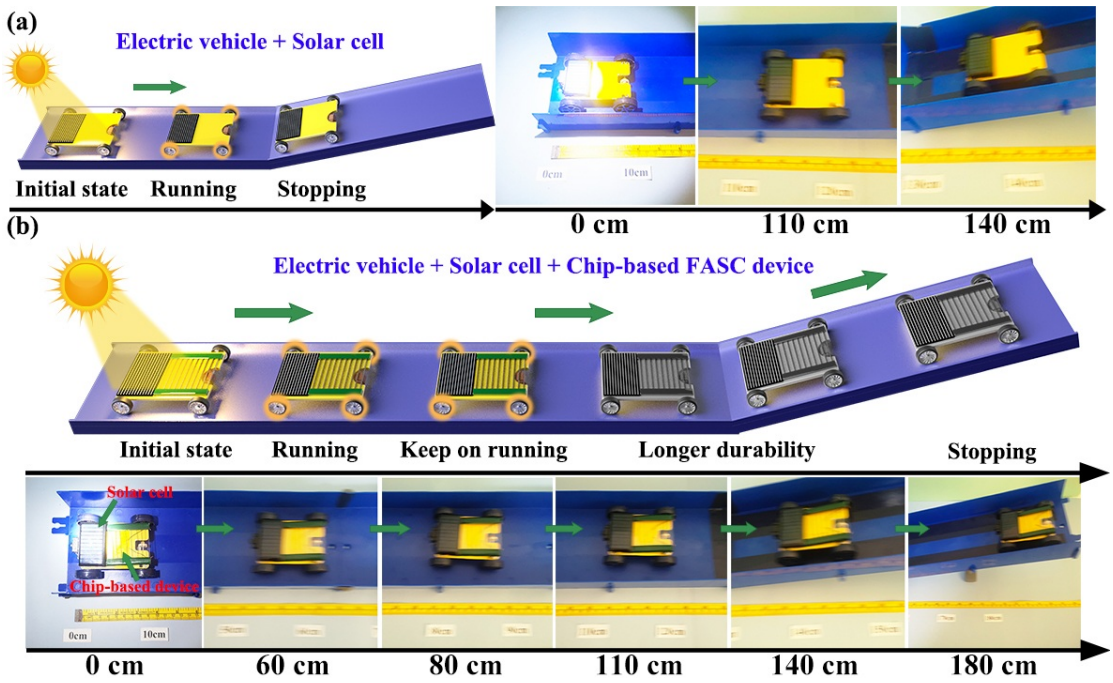

Fig. S27. Schematic and photographs of the running of the electric car with solar cell and self-powered system. (a) Schematic and photographs of the movements of the electric car with solar cell only. (b) Schematic and photographs of the movements of the electric car with the self-powered system, including chip-based FASC device and solar cell. Photo credit: (a and b) Jingxin Zhao, University of Macau.

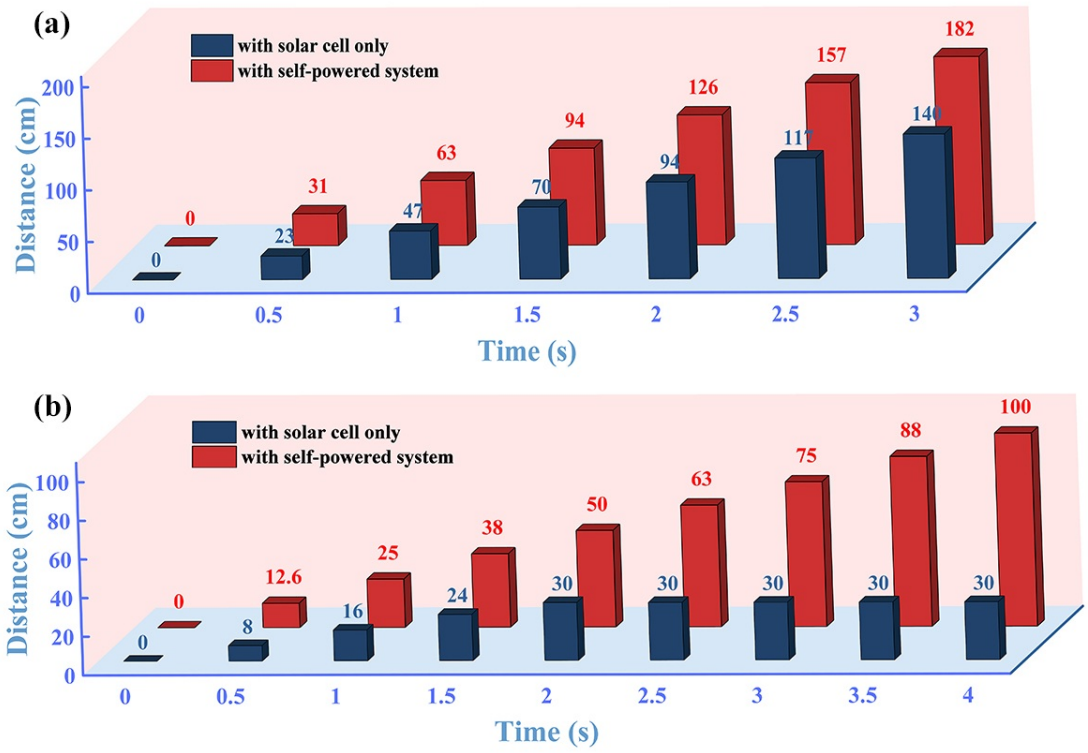

Fig. S28. The relationship between the running distance and time of the mechanical configuration. (a) The electric car with solar cell only and with a self-powered system. (b) The sightseeing cable car with solar cell only and with self-powered system.

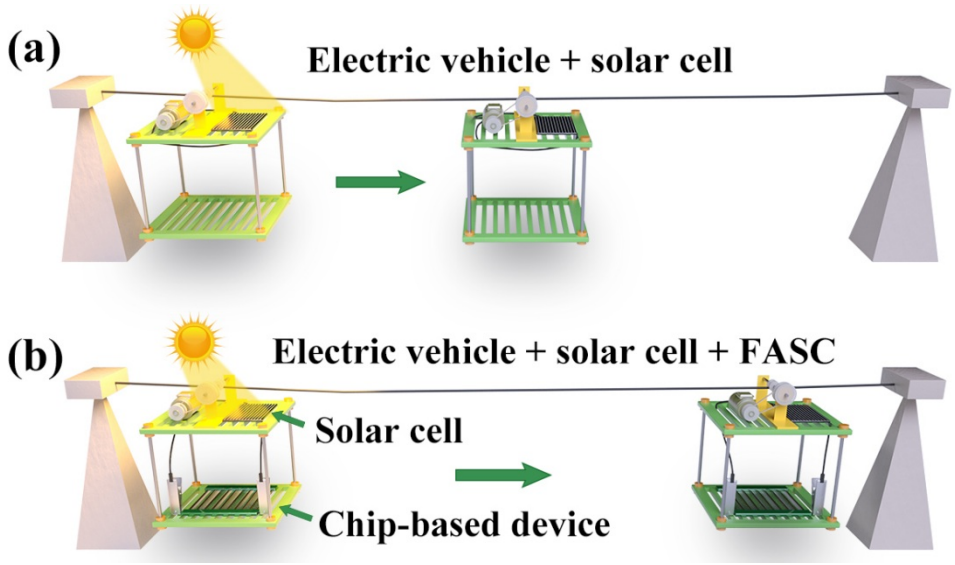

Fig. S29. Schematic diagram of the movements of the sightseeing cable car with solar cell and self-powered system. (a) Schematic diagram of the running of sightseeing cable car with solar cell only, the sightseeing cable car can run a short distance without extra energy storage. (b) Schematic diagram of the running of sightseeing cable car with the self-powered configuration including chip-based FASC device and solar cell, the sightseeing cable car can run the long-distance with energy storage, demonstrating the longer durability.

Fig. S30. The digital photo of the self-energy monitoring system. Photo credit: Hongyu Lu, Xi'an University of Technology.

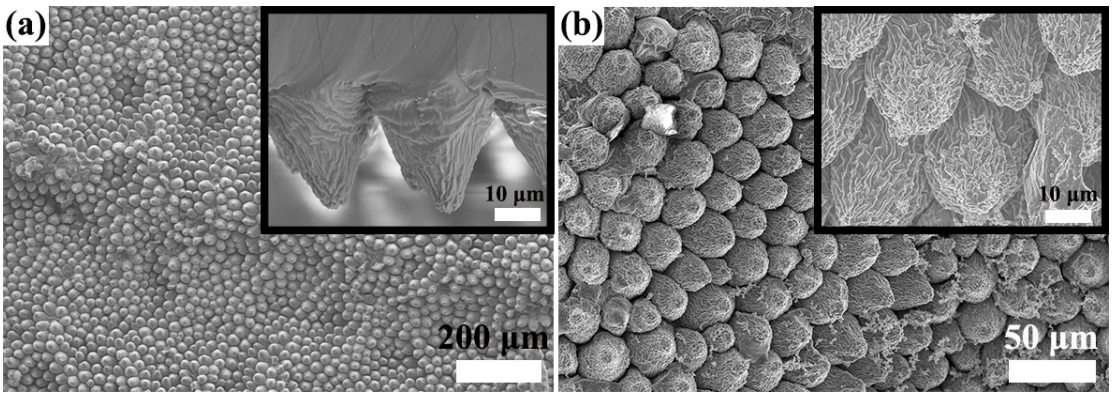

Fig. S31. SEM images of the obtained multiscale structured materials. (a) PDMS and (b) PPy/PDMS stamps.

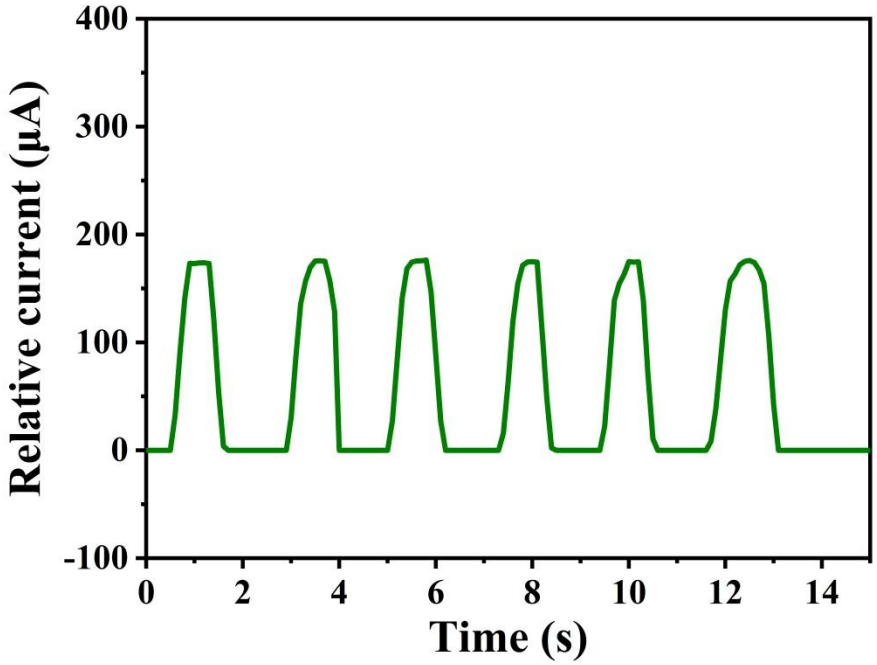

Fig. S32. Response signal of the pressure sensor under the pressure load.

Table S1. Comparison of the 3D printing coaxial FASC device with the reported FASC device.

Device configuration	Electrode materials	Mass loading	Specific capacitance	Energy density	Power density	Reference
coaxial	MnO_2@MWCNT fiber	/	10.9 F cm^{-3} 10.3 F g^{-1}	1.51 mWh cm^{-3} 1.4 Wh kg^{-1}	52.9 mW cm^{-3} 49.9 W kg^{-1}	3
parallel	$Ni(OH)_2$@rGO/Ni wire-rGO/Ni wire	/	1.9 F cm^{-3}	0.8 mWh cm^{-3}	3.4 W cm^{-3}	5
parallel	N-Doped graphene fiber	/	95.1 mF cm^{-2} 14.9 F cm^{-3}	25.6 μWh cm^{-2} 10.0 mWh cm^{-3}	550.2 μW cm^{-2} 216.0 mW cm^{-3}	6
twisted	FCNO NWAs/GF-CNR/GF		61.6 mF cm^{-2} 16.4 F cm^{-3}	16.8 μWh cm^{-2} 4.5 mW cm^{-3}	69.9 μW cm^{-2} 18.7 mW cm^{-3}	7
coaxial	MnO_2@CNT fiber/Ppy@CNT film	/	60.4 mF cm^{-2} 9.5 F cm^{-3} 7.7 F g^{-1}	18.9 μW h cm^{-2} 3.0 mW h cm^{-3} 2.4 Wh kg^{-1}	522.0 μW cm^{-2} 82.5 mW cm^{-3} 0.8 W kg^{-1}	8
Parallel	PHCFs/PANi	2.4 mg cm^{-1} 9.0 mg cm^{-2} 710.1 mg cm^{-3}	622.0 mF cm^{-2} 49.1 F cm^{-3} 69.1 F g^{-1}	55.3 μW h cm^{-2} 1.6 mWh cm^{-3} 6.1 Wh kg^{-1}	447.0 μW cm^{-2} 12.0 mW cm^{-3} 44.4 W kg^{-1}	9
coaxial	$ZnCo_2O_4$@Zn-Co-S/CNTFs//H-Co_3O_4@CoNC/CNTFs	/	117.2 mF cm^{-2}	32.0 μW h cm^{-2}	698.4 μW cm^{-2}	10

twisted	rGO/CNT-NiCo-BOH Yarn	/	79.6 mF cm^{-2} 5.3 F cm^{-3} 2.2 F g^{-1}	21.7 μWh cm^{-2} 1.4 mWh cm^{-3} 0.6 Wh kg^{-1}	349.8 μW cm^{-2} 23.2 mW cm^{-3} 9.5 W kg^{-1}	11
twisted	V_2O_5/SWCNTs-VN/SWCNTs	/	116.2 mF cm^{-2} 18.6 F cm^{-3}	41.3 μWh cm^{-2} 6.6 mWh cm^{-3}	480.0 μW cm^{-2} 76.8 mW cm^{-3}	14
coaxial	CNT yarn or sheet//Ti NTs/Ti wires	/	1.8 mF cm^{-2}	0.2×10^{-3} mW h cm^{-3}	0.01 mW cm^{-3}	16
twisted	CCCH@NiCoLDH NWAs@Au–CuO/Cu	0.1 mg cm^{-1} 1.596 mg cm^{-2} 318.471 mg cm^{-3}	147.2 mF cm^{-2}	66.2 μW h cm^{-2}	2.9 mW h cm^{-2}	17
parallel	MnO_2 NAs/CF-G/CF	/	4.50 mF cm^{-2}	1.41 μWh cm^{-2}	48.5 μW cm^{-2}	18
parallel	PEDOT/MnO_2-C@Fe_3O_4	/	60.0 mF cm^{-2} 7.2 F cm^{-3} 33.5 F g^{-1}	33.5 μW h cm^{-2} 4.0 mWh cm^{-3} 18.6 Wh kg^{-1}	600.0 μW cm^{-2} 72.0 mW cm^{-3} 334.5 W kg^{-1}	51
twisted	N-doped rGO/CNT fiber	/	5.5 mF cm^{-2} 2.6 F cm^{-3}	3.0 μW h cm^{-2} 0.4 mWh cm^{-3}	51.8 μW cm^{-2} 3.0 W cm^{-3}	52
coaxial	PEDOT-S: PSS fiber	/	93.1 mF cm^{-2}	8.3 μW h cm^{-2}	400.0 μW cm^{-2}	53

parallel	rGO-Ni yarns	/	72.1 mF cm^{-2}	1.6 μWh cm^{-2}	145.7 μW cm^{-2}	54
twisted	CNT/graphene/ PANi	/	273.7 mF cm^{-2} 91.2 F cm^{-3} 137.5 F g^{-1}	24.3 μW h cm^{-2} 8.1 mW h cm^{-3} 12.2 Wh kg^{-1}	673.5 μW cm^{-2} 224.3 mW cm^{-3} 338.4 W kg^{-1}	55
parallel	MnO_2/Porous Ni fiber	/	211.8 mF cm^{-2}	18.8 μWh cm^{-2}	16.3 mW cm^{-2}	56
3D printing coaxial FASC device	**V_2O_5 NWs/MWCNTs//VN NWs/MWCNTs**	**2.1 mg cm^{-1} 16.4 mg cm^{-2} 1639.4 mg cm^{-3}**	**152.7 mF cm^{-2} 27.8 F cm^{-3} 59.3 F g^{-1}**	**54.3 μWh cm^{-2} 9.9 mWh cm^{-3} 21.1 Wh kg^{-1}**	**801.4 μW cm^{-2} 4000.1 mW cm^{-3} 8000.6 W kg^{-1}**	**This Work**